

Effects of Interface Bonding on the Residual Stresses in Cold-Sprayed Al-6061: A Numerical Investigation

Enqiang Lin¹ · Qiyong Chen¹ · Ozan C. Ozdemir¹ · Victor K. Champagne² · Sinan Müftü¹

Submitted: 19 June 2018 / in revised form: 15 November 2018 / Published online: 23 January 2019
© ASM International 2019

Abstract A contact model that accounts for interfacial cohesion and thermal conduction is developed to investigate the influence of bonding on the final residual stresses build-up in cold spray. The residual stress evolution in the cold-sprayed Al-6061 coating on an Al-6061 substrate is investigated via three-dimensional single-particle and multi-particle impact simulations. It is shown that the interface bonding mainly affects the local residual stress distribution near the interfaces. The residual stresses are largely due to the kinetic peening and bonding effects. The thermal cooling has negligible influence. In general, this work finds that peening introduces compressive stress, while bonding causes relaxation. The balance between the peening and the bonding effects, which depends strongly on the local bonding environment, determines the final residual stress in the system. This work suggests that the interface bonding should be considered as one of the

essential factors in numerical modeling of the residual stresses evolution in cold spray.

Keywords aluminum coating · cold spray · interface bonding · numerical simulation · residual stress

Instruction

Cold spray (CS) is a solid-state material deposition process in which micron-sized powder particles, which are accelerated up to speeds of 300–1200 m/s in a supersonic gas stream, impact and bond onto a metallic substrate forming a functional coating. The particle bonding is a critical factor that influences the engineering implementation of CS. It is now well recognized that successful bonding in CS is associated with severe plastic deformation of the particles during impact and is achieved only when particle velocities exceed a critical velocity, which depends on the material properties and process conditions (Ref 1, 2).

A distinct feature of the CS is the compressive residual stress that builds up in the coating. The compressive nature of the residual stress is helpful for the fatigue and strength characteristics of the coated materials (Ref 3, 4). The residual stress results from the particle/substrate and particle/particle interactions during deposition and is closely related to the resulting interface bonding. A number of factors can influence the residual stress level developed in the CS coating, including the peening effect due to the constant bombardment of particles, the annealing effect that is introduced by the supersonic hot gas stream, and the thermal relaxation at the bonding interface due to the cooling from the temperature levels that rise during CS. Among these factors, understanding, predicting and controlling the relationships between the residual stress and the

This article is an invited paper selected from presentations at the 2018 International Thermal Spray Conference, held May 7–10, 2018, in Orlando, Florida, USA, and has been expanded from the original presentation.

Electronic supplementary material The online version of this article (<https://doi.org/10.1007/s11666-019-00827-7>) contains supplementary material, which is available to authorized users.

✉ Enqiang Lin
en.lin@northeastern.edu

✉ Sinan Müftü
s.muftu@neu.edu

¹ Department of Mechanical and Industrial Engineering, Northeastern University, Boston, MA 02115, USA

² United States Army Research Laboratory, Aberdeen Proving Ground, MD 21005, USA

individual particle bonding process requires careful investigation. As a result, investigating the particle bonding and the corresponding residual stress formation is the focus of this work.

Most of the recent studies on CS are dedicated to reveal the bonding mechanisms and to predict the critical velocities of various particle/substrate material systems. Relatively few experimental or simulation studies focus on investigating the residual stress developed by CS. Three types of experimental approaches are used to quantify the residual stresses. Using a curvature-based measurement method, Arabgol et al. (Ref 5) analyzed the influence of various parameters (e.g., coating and substrate thickness, etc.) on the residual stress built-up in spraying copper on copper and steel. They found that the overall heat input and associated thermal history play major roles in determining the final in-plane residual stress. Suhonen et al. (Ref 6) investigated the effects of substrate materials and substrate pretreatment on the deposition, thermal and final residual stresses formed during CS deposition of Al, Cu and Ti coatings. Compressive, neutral and tensile stresses, which depend strongly on the substrate/coating material combination and the surface preparation, were observed in their tests. Using x-ray diffraction (XRD), Ghelichi et al. (Ref 3) measured the residual stress of Al5052 coated with pure Al and Al7075 powders and studied their effects on the fatigue crack initiation. Their results revealed a 30% improvement in the fatigue strength for the case of Al7075 coating. Rokni et al. (Ref 7) analyzed the residual stresses of cold-sprayed Al6061 coating on Al6061 substrate, observing a compressive residual stress state in the cold spraying direction while a tensile residual stress in the transverse direction near the substrate/coating interface. Shayegan et al. (Ref 8) evaluated the residual stress in magnesium AZ31B alloy as-coated with Al powders, observing a compressive stress (-25 MPa) at the coating surface, which rises first (-54 MPa) and fall later (0 MPa) through the thickness into the substrate. Luzin et al. (Ref 9) studied residual stress profiles in Cu- and Al-coated samples by neutron diffraction. They demonstrated that residual stress magnitude is mainly determined by the kinetic peening rather than the thermal effect. Later, through the investigations of cold-sprayed Al and Al alloys (Al7075 and Al6061) on Mg substrate, they (Ref 10) concluded that the accumulation of residual stresses depends more on the coating material properties (e.g., plastic deformation resistance) than the processing parameters (e.g., impact temperature and pressure). Rech et al. (Ref 11) compared the three different residual stress measurement methods mentioned here, when investigating the influence of substrate temperature on the residual stress. They found that the stress values measured by the curvature and the XRD methods are in good agreement with each other. Though

different measurement techniques and material combinations were used in the work reported above, they all confirm that mainly compressive residual stresses develop as a result of cold spray and that the stress magnitudes are affected by various material- and system-related factors.

As an effective supplement to experimental investigations, finite element (FE) analysis is also employed to study the residual stresses and the factors that influence them in cold spray. Shayegan et al. (Ref 8) used both single- and multi-particle impact FE models to study the influences of particle size, shape and velocity on the evolution of residual stress profile developed in coating Al powders on magnesium AZ31B alloy. Saleh et al. (Ref 12) also used single- and multi-particle impact models, but with the smooth particle hydrodynamics (SPH) formulation, to simulate the deposition process of Al6061 particles on Al6061 substrate and study the associated residual stress profiles. Ghelichi et al. (Ref 13) employed the multi-particle impact FE model, where particle size, velocity, temperature and impact positions were determined by using analytical distribution models, to analyze the particle peening and gas annealing effects on the residual stress developed in Al5050 and Al6061 substrates that were coated with Al7075 powders. Li et al. (Ref 14) used the constrained single- and multi-particle impact FE models with Eulerian formulation to explore the interfacial residual stress distributions in Cu particle deposited on Cu or Al substrates. Although the simulated stresses in these FE analyses are to some extent comparable to the reported experimental values, one limitation in these simulations is that the particle bonding and deposition processes, which may strongly affect the final residual stresses, are not modeled. Therefore, in an attempt to solve this limitation, an interface contact model that accounts for both the cohesion and interfacial thermal conduction effects is developed in this work. Evolution of residual stresses during CS of Al6061 particles on Al6061 substrate is then investigated.

The remainder of the paper is organized as follows. The three-dimensional (3D) single- and multi-particle impact simulations as well as the material and interface contact models used in the simulations are described in [Numerical Simulations and Contact Model](#) section. The simulated evolution of the residual stresses is demonstrated and analyzed in [Results and Discussions](#) section. The main findings are summarized in [Conclusions](#) section.

Numerical Simulations and Contact Model

Finite Element Model

Impact of particles on a flat substrate is simulated in a Lagrangian reference frame by using the commercially

available FE analysis software ABAQUS/Explicit (Ref 15). The Lagrangian method is used as it provides a unique way to model the interface contact interactions for the particle bonding. Three different cases are considered: *i*) single-particle impact on a substrate, *ii*) overlapping impacts of six particles, and *iii*) random impacts of multiple particles, as depicted in Fig. 1. In these models, the substrate is modeled as a cylinder with a radius of 250 μm and height of 130 μm . Different partitions are created in the substrate to obtain an optimized mesh distribution at the non-impact region to reduce the computational costs. One common feature in high-velocity impact simulations is the generation and trapping of stress waves in the model that may bring up numerical stability issues. Therefore, a layer of *infinite elements* is introduced on the bottom and peripheral surfaces of the substrate to dampen the stress waves and to reduce the interfacial fluctuations that could affect the particle bonding. As these infinite element layers also serve as the fixed boundary constraints in the substrate, no additional mechanical boundary conditions are applied to the model.

Spherical particles with 19 μm diameter (d_p) are used in single- and six-particle impact simulations. It is noted that the overlapping impact of six particles is just an idealized model to understand and illustrate the importance of interface bonding on the residual stress built-up. The intention is not to mimic the random and layer-by-layer deposition found in CS. The particle and the substrate are assumed to be at room temperature (293 K). The assumption of room temperature substrate is reasonable when the CS-nozzle moves fast across the substrate. The effects of the elevated particle temperatures will be investigated separately. A time interval of 50 ns is simulated for each individual impact. Different impact velocities varying in the range of 850–1050 m/s are investigated in the single-particle impact analyses. While a fixed impact velocity of

950 m/s is used in the six-particle impact cases. In both simulation approaches, the particle/substrate and particle/particle interactions are simulated by using a cohesive surface contact model that is introduced in the following section.

Particle impact conditions are determined by using computational fluid dynamics for the multi-particle random impact simulations (Ref 16). A typical particle size distribution as measured by using a Microtrac laser powder analyzer is shown in Fig. 2(a). The cumulative probability distribution of the particle size is estimated by a log-normal function:

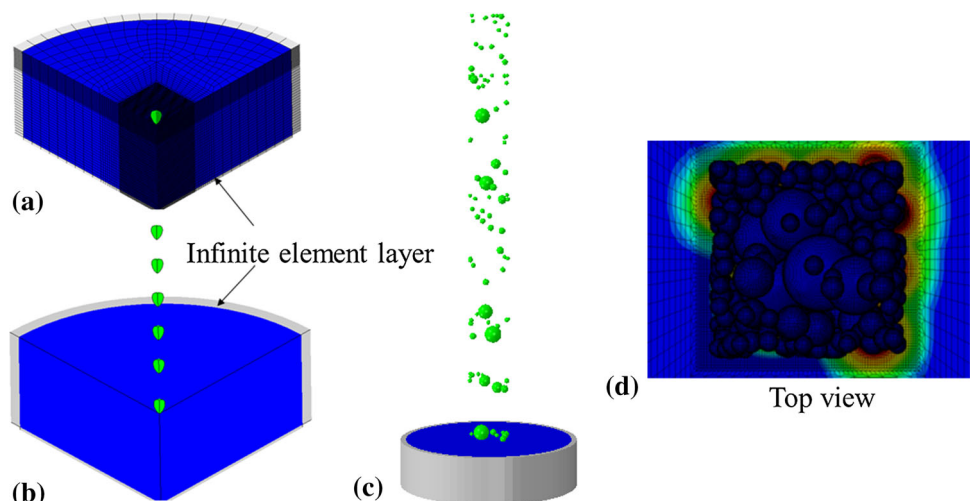
$$f(d_p) = 50 \left[1 + \operatorname{erf} \left(\frac{\ln(d_p) - \ln(\bar{d}_p)}{\sigma_{\log} \sqrt{2}} \right) \right] \quad (\text{Eq 1})$$

with the parameters $\bar{d}_p = 37.0$ and $\sigma_{\log} = 0.36$. The supersonic flow of He gas through a converging–diverging nozzle (Fig. 2b), with conditions of 48.3 bar at 400 °C on the supply side, is simulated. The dependence of the impact velocity V and temperature T on the particle diameter d_p are determined from the CFD simulations, as shown in Fig. 2(c) and (d) and curve fitted as follows:

$$\begin{aligned} V(d_p) &= 1455.5e^{-0.011d_p} \\ T(d_p) &= 239.42e^{0.008d_p} \end{aligned} \quad (\text{Eq 2})$$

One hundred particles with random sizes, $d_p = 11\text{--}78 \mu\text{m}$, were generated, as shown in Fig. 1(c). Equation 1 and 2 is then used to find the corresponding impact velocity to be in the range of 600–1300 m/s for $T = 293 \text{ K}$. Though the particle impact positions on the substrate can be determined from the CFD analysis, the uniform distribution assumption is adopted in this work to confine the impacted particles within the densely meshed central region of the substrate. A duration of $\sim 120 \text{ ns}$ is used for each individual impact to reduce the computational costs. The

Fig. 1 Mesh configuration and finite element model of (a) single-particle impact; (b) six-particle overlap impact; (c) and (d) multi-particle random impact



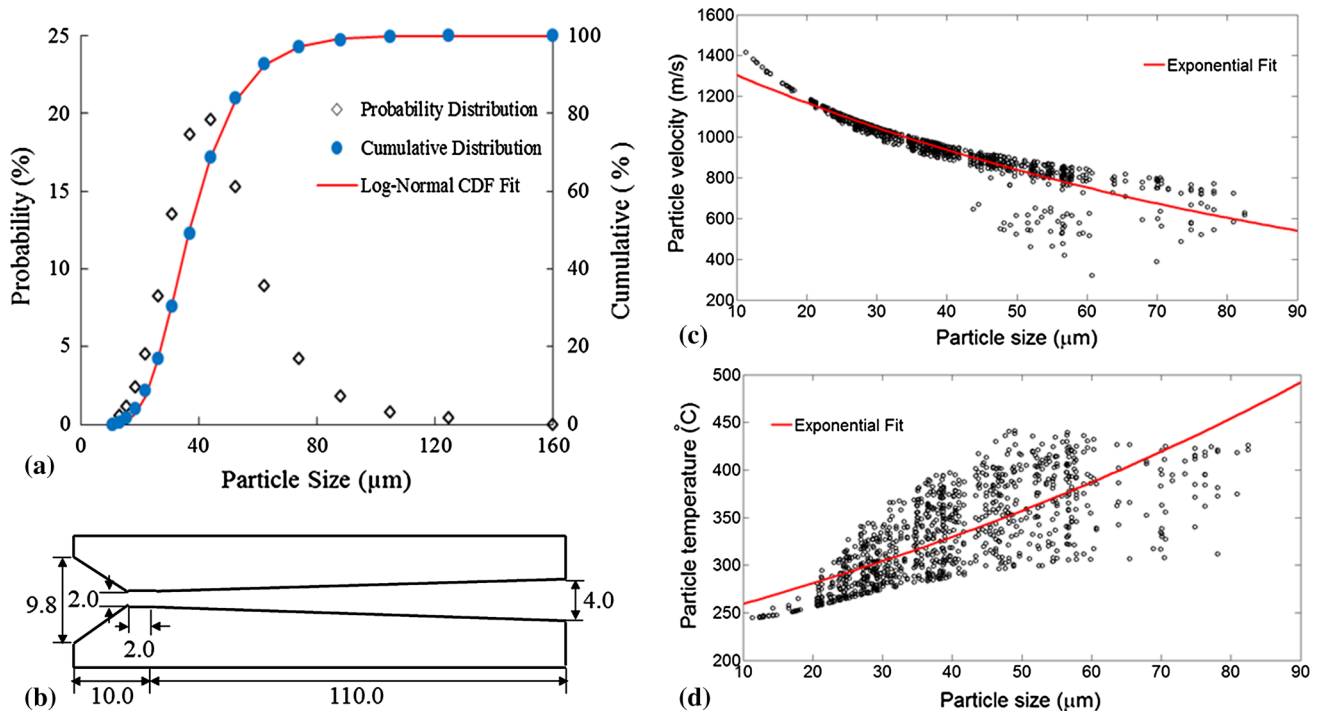


Fig. 2 (a) Particle size distribution and cumulative distributions measured by Microtrac powder analyzer. Particle size dependence of (c) the impact velocity and (d) temperature calculated from the CFD simulation (Ref 15) with nozzle dimension (b) (in unit mm)

particles and the substrate are meshed with hexahedral elements of size $d_p/40$ and $d_p/20$, respectively. C3D8RT element with distortion and enhanced hourglass controls is used in the simulations for the thermomechanical analysis. The material nonlinearity and large deformation effects are included in the simulations.

Material Model

Cold spray of Al6061 powders on the same substrate is simulated. The material is assumed to be isotropic with the properties which are listed in Table 1. The bilinear Johnson–Cook (JC) plasticity model (Ref 17) is used to describe the rate and temperature dependence of the material behavior:

$$\sigma = \left(A + B \dot{\epsilon}_p^n \right) \left[1 + C \ln \left(\frac{\dot{\epsilon}_p}{\dot{\epsilon}_0} \right) \right] \left[1 - \left(\frac{T - T_r}{T_m - T_r} \right)^m \right] \quad (\text{Eq 3})$$

$$C = \begin{cases} C_1 & \text{and } \dot{\epsilon}_0 = 1 \quad \text{if } \dot{\epsilon}_p \leq \dot{\epsilon}_c \\ C_2 & \text{and } \dot{\epsilon}_0 = \dot{\epsilon}_c \quad \text{if } \dot{\epsilon}_p > \dot{\epsilon}_c \end{cases} \quad (\text{Eq 4})$$

where σ is the flow stress, $\dot{\epsilon}_p$ is the strain rate, $\dot{\epsilon}_0$ is the reference strain rate, T_r is a reference temperature, T_m is the melting temperature of the material, A , B , n and m are the model parameters, C_1 and C_2 are coefficients that describe the additional increase in flow stress when the applied $\dot{\epsilon}_p$ is greater than the critical plastic strain rate $\dot{\epsilon}_c$. The

parameters of the bilinear JC model (Ref 18) were obtained by least-squares curve fitting of the single-particle impact simulation results to the shapes of the deformed particles measured in advanced laser-induced projectile impact (α -LIPIT) tests (Ref 19). The fraction of plastic energy converted into heat is assigned to be 0.9 (Ref 20). The corresponding thermal response of the material is then defined by its temperature-dependent thermal properties, such as specific heat, thermal conductivity and thermal expansion (Ref 21).

Material failure, which has been tested to be one of the important factors that affect the numerical accuracy on the modeling of high-velocity impact problems (Ref 22), is also considered in this paper. Johnson–Cook damage model (Ref 23), which is widely used in the projectile penetration simulations, is employed as the ductile failure initiation criterion:

$$\bar{\epsilon}_D^p = \left[d_1 + d_2 \exp \left(-d_3 \frac{p}{q} \right) \right] \left(1 + d_4 \ln \left(\frac{\dot{\epsilon}_p}{\dot{\epsilon}_0} \right) \right) \left(1 + d_5 \left(\frac{T - T_r}{T_m - T_r} \right) \right) \quad (\text{Eq 5})$$

where $\bar{\epsilon}_D^p$ is the equivalent plastic strain at damage initiation, p/q is the stress triaxiality, d_1 – d_5 are empirical material parameters reported by Ref 24 for Al6061. The failure parameter d_1 was adjusted slightly in order to better reflect the material damage initiation at the periphery of the particle–substrate contact interface. After the onset of damage initiation, the material (or flow stress) is assumed

Table 1 Material properties for A16061 alloy

Properties	Parameter (unit)	Value
General	Density, ρ (kg/m ³)	2700(a)
	Specific heat, C_p (J/kg K)	1009(a)
	Thermal conductivity (W/m K)	155(a)
	Thermal expansion ($10^{-6}/K$)	22.3(a)
	Melting temperature, T_m (K)	925
	Inelastic heat fraction, β	0.9
Elastic	Elastic modulus, GPa	69.11(a)
	Poisson's ratio	0.331(a)
Plastic (Johnson–Cook plastic model)	A, B, n, m (MPa, MPa)	270, 154.3, 0.239, 1.42
	$C_1, C_2, \dot{\epsilon}_c$	0.002, 0.0029, 597.2
	Reference strain rate, $\dot{\epsilon}_0$ (1/s)	1.0
	Reference temperature, T_r (K)	293
Failure initiation	d_1, d_2, d_3, d_4, d_5	– 0.57, 1.45, 0.47, 0.011, 1.6
Failure evolution	Displacement at failure, \bar{u}_f^p , μm	0.1
Interface contact	Compressive stiffness, k_{com} (MPa/mm)	Default(b)
	Cohesive stiffness, k_{coh} (MPa/mm)	1×10^{11}
	Cohesive strength, σ_0 (MPa)	325
	Damage evolution energy, G (J/m ²)	1.0
	Gap conductance, k_{gap} (W/m ² K)	$155/\delta_{max}$

(a) Temperature-dependent properties. The values at room temperature (293 K) are shown. Data are taken from MPDB software (Ref 19)

(b) Default means k_{com} is determined automatically by ABAQUS

to degrade linearly with the effective plastic displacement \bar{u}^p until its final failure at \bar{u}_f^p . Thus, when \bar{u}^p reaches \bar{u}_f^p (Table 1), the underlying material loses its load carrying capacity and the associated elements are removed from the models. When the material is removed from the contact interface, the interior material is exposed and becomes involved in the bonding process. This is similar to the real cold spray condition where the surface oxide layers are broken exposing the interior of the particle. The material jetting observed experimentally (Ref 25) is thus realized in the simulations by using the material damage approach.

Interface Contact Model

In order to model the interface bonding during particle impact, a cohesive surface contact model is proposed in this paper. The cohesive traction σ_t is defined in vector form as follows:

$$\sigma_t = \begin{Bmatrix} \sigma_t^n \\ \sigma_t^{eq} \end{Bmatrix} = \begin{bmatrix} k_n & 0 \\ 0 & k_t \end{bmatrix} \begin{Bmatrix} \delta_n \\ \delta_{eq} \end{Bmatrix} = K\delta \quad (\text{Eq 6})$$

where σ_t^n is the normal and σ_t^{eq} is the tangential component of the cohesive traction vector, k_n and k_t are the associated stiffness values for the normal and tangential displacements δ_n and $\delta_{eq} = \sqrt{\delta_{t1}^2 + \delta_{t2}^2}$ (t_1 and t_2 are the two

tangential directions) at the interface, respectively. According to the interface contact status (compressive or cohesive) in the normal direction (δ_n), as shown schematically in Fig. 3, σ_t^n and σ_t^{eq} can further be defined as follows:

$$\sigma_t^n = \begin{cases} k_{com}\delta_n & \text{if } \delta_n \leq 0 \\ k_{coh}\delta_n & \text{if } 0 < \delta_n \leq \delta_{nc} \\ (1 - D(\delta_n))k_{coh}\delta_n & \text{if } \delta_n > \delta_{nc} \end{cases} \quad (\text{Eq 7})$$

$$\sigma_t^{eq} = \begin{cases} k_{com}\delta_{eq} & \text{if } \delta_n \leq 0 \\ 0 & \text{if } \delta_n > 0 \end{cases} \quad (\text{Eq 8})$$

When the normal separation is negative ($\delta_n \leq 0$), the interface is in compression and the contact stiffness $k_n = k_t = k_{com}$ is used to determine the compressive contact stress in the normal and tangential directions. When the separation is positive ($\delta_n > 0$), cohesive stresses are active in the interface. The corresponding traction is determined by using the contact stiffness $k_n = k_{coh}$ and $k_t = 0$ (Eq 8 and 9). The cohesive traction has a bilinear character such that if δ_n is greater than a critical separation distance δ_{nc} , the stiffness k_{coh} is gradually degraded due to the cohesive damage $D(\delta_n)$ that is determined through the cohesive strength σ_0 , cohesive damage energy G and δ_n (see Fig. 3). In this work, the cohesive strength σ_0 , which to some extent reflects the bonding strength, was chosen on the

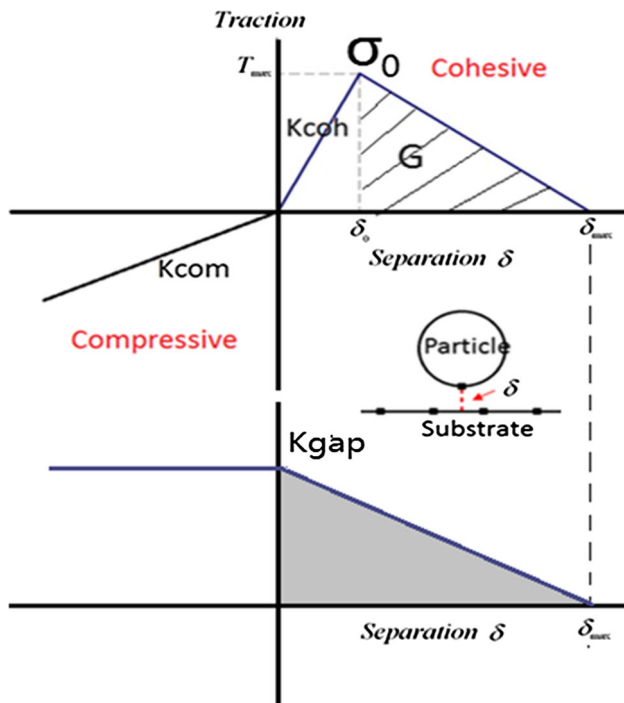


Fig. 3 Schematic diagram of the proposed cohesive surface contact model that accounts for both mechanical and thermal interactions during the particle impact

basis of the tensile strength value of Al6061. The cohesive energy G , which can be treated as the critical energy release rate for particle debonding, was selected by referring to the grain boundary energy of Al6061 (Ref 26–28).

During the particle and substrate contact, a thermal gap conductance k_{gap} is also considered in the proposed model. The heat flux, \dot{q} , in the contact interface is assumed to be proportional to the temperature difference, and it is expressed as follows:

$$\dot{q} = k_{\text{gap}}(T_A - T_B) \quad (\text{Eq 9})$$

where the gap conductance degrades with increasing separation as follows:

$$k_{\text{gap}} = \frac{k_{\text{con}}}{\delta_{\text{max}}} (1 - \delta_n / \delta_{\text{max}}) \quad (\text{Eq 10})$$

where k_{con} is the thermal conductivity of the solid body which can only take positive values or zero. This linear dependency of k_{gap} on the normal separation δ_n is schematically plotted in Fig. 3. When the separation is positive ($\delta_n > 0$), k_{gap} decreases from the maximum $k_{\text{con}} / \delta_{\text{max}}$ to zero with increasing δ_n . When the separation is negative ($\delta_n \leq 0$), k_{gap} is assumed to be temperature and pressure independent and kept at its maximum for simplicity. The parameters for the proposed model are listed in Table 1, where $k_{\text{con}} = 155 \text{ W/(m K)}$ at $T = 293 \text{ K}$ for Al6061 is used to determine the maximum k_{gap} . These

parameters are chosen to reproduce the experimental critical velocity of $\sim 840 \text{ m/s}$ for bonding Al6061 particle on Al6061 substrate (Ref 19). The contact model is implemented into ABAQUS/Explicit through the user subroutine VUINTERACTION.

Results and Discussions

Residual Stress in Single-Particle Impact

Single-particle impact simulations are performed to investigate the effects of interface bonding on the computed residual stresses after particle deposition. The minimum and maximum principal stresses are used to characterize the residual stresses in these simulations to eliminate the directionality. The implementation of the surface model is verified to have the same bilinear cohesion traction during particle separation as that plotted in Fig. 3 (see “Appendix”). In this section, the objective is to compare the simulated residual stresses obtained with the proposed surface contact model and those obtained with the infinitely strong cohesion model (or rough contact) and the built-in surface-based cohesive model in ABAQUS (Ref 15). Infinitely, strong cohesion implies that the particle–substrate interface is not allowed to separate after contact. The built-in surface-based cohesive model shares a similar bilinear traction–separation relationship as the proposed contact model (see Fig. 3). However, its implementation is not verified due to the black box feature of the built-in model.

Variation of the von Mises stress distribution in the system at $t = 200 \text{ ns}$ for particle impact velocities of 850, 950 and 1050 m/s is presented in Fig. 4. Note that these velocities are above the experimentally observed critical velocity values of $\sim 840 \text{ m/s}$ (Ref 19). Both the proposed and built-in contact models mainly affect the stress distributions near the interface region. The differences in the stress distributions predicted by the three models are small far from the contact interface, especially in the substrate. For the model with enforced bonding, the stress distributions are symmetric with respect to the central axis. They vary relatively smoothly and appear continuous across the interface. In contrast, the cohesion-based contact models predict discontinuity along the interface. This is attributed to the non-uniform bonding along the interface. In fact, further check of the contact interfaces (Fig. 4a–c) indicates that the peripheral region generally bonds better than the center region (e.g., with small visible interface gaps at $V_p = 850 \text{ m/s}$). The stress distribution of the built-in cohesion model has difficulty with symmetry, especially in the particle. This asymmetry is found to be related to the node penetration at the contact interface, where some of the

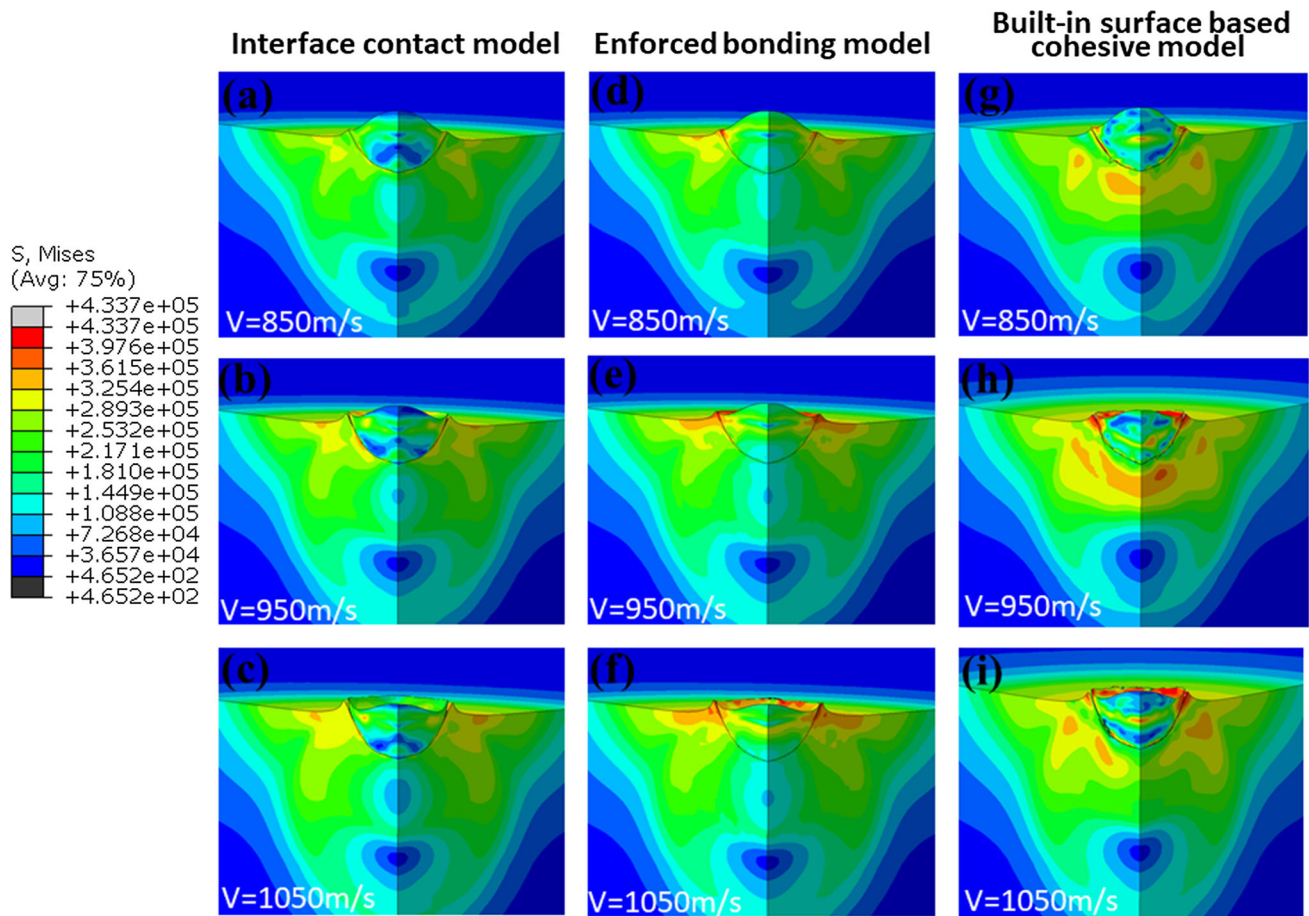


Fig. 4 Von Mises stress distribution in single-particle impact at $t = 200$ ns for (a)–(c) FE model with proposed surface contact method; (d)–(f) FE model with enforced bonding model and (g)–(i) FE model with built-in surface-based cohesive model

particle surface nodes are observed to unexpectedly penetrate into the substrate during the impact, leading to an asymmetric contact distribution on the interface. On the other hand, the proposed cohesion model is much more effective in keeping the results symmetrical.

The variation of the minimum principal stress along the symmetry axis is shown in Fig. 5(a)–(c), for the three modeling approaches. The minimum principal stress is used as a metric for the residual stresses in the material. It is seen in Fig. 5(a) that the minimum principal stresses on both sides of the particle and the substrate near the contact interface are significantly reduced with the proposed contact model. This implies that the interface bonding has a relaxing effect, on the developed compressive residual stresses during particle impact relative to the enforced bonding model. Comparing the depths of influence, the interface bonding is found to have a greater effect on the particle than the substrate (Fig. 5a). Thus, it is inferred that interface bonding will have a stronger effect on the residual stresses in the coating than in the substrate. The local residual stress relaxation effect as a result of the cohesive traction is also observed in the built-in model in Fig. 5(c).

However, due to the node penetration, the relaxation effect seems to be greater in the built-in model since a smaller compressive residual stress in the particle and a larger compressive residual stress in the substrate region near the interface are observed.

The stress history of the particle's south pole during impact is presented in Fig. 5(c). It is observed that the impact event and the associated residual stress built-up generally can be divided into three steps: the initial shock step ($t < 5$ ns), the transient peening and bonding step ($5 \text{ ns} < t < 50$ ns) and the steady-state cooling step after particle bonding ($t \geq 50$ ns). The shock and peening steps result in a compressive residual stress in the system. However, due to the cohesive tractions, the interface bonding relaxes the compressive residual stress. Therefore, smaller minimum principal stresses are observed in the simulations with cohesive tractions than those with enforced bonding (Fig. 5c). The thermal cooling step seems to have negligible effect on further relaxing the developed compressive residual stress in current simulations. This is attributed to two factors. First, the particle and the substrate are initially at the same temperature, and

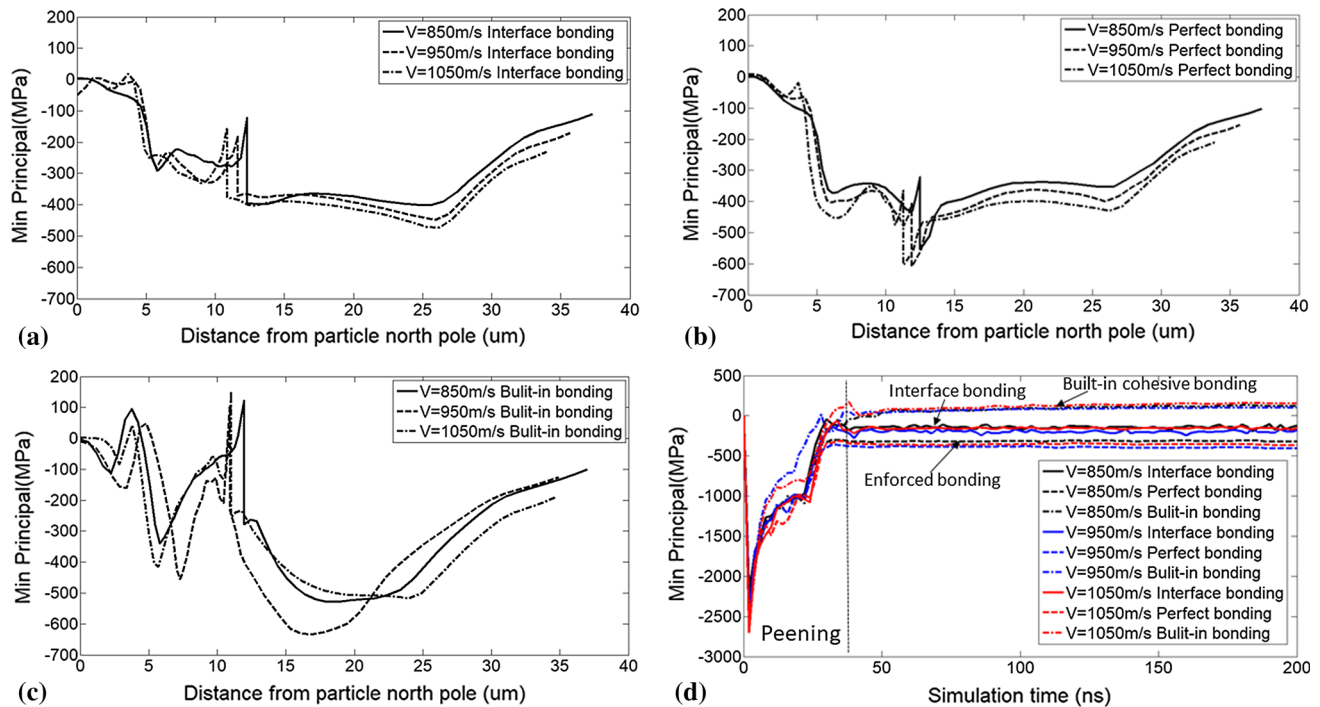


Fig. 5 (a)–(c) Through-thickness minimum principal stress distribution along the symmetry axis measured from the north pole node of the particle for (a) the proposed interface contact model; (b) the

enforced contact model and (c) the ABAQUS built-in surface-based cohesive model. (d) The minimum principal stress evolves with simulation time for the south pole element in particle

second, they have the same thermomechanical properties (e.g., thermal expansion). Under these conditions, the temperature difference between the particle and substrate due to plastic heating does not appear to be sufficient to bring about either a quenching effect or a thermal mismatch effect. Therefore, a relatively stable compressive residual stress is observed in Fig. 5(d) during the thermal cooling step. Effects of initial temperature and temperature difference between particle and substrate on the residual stress development will be systematically investigated in future work.

Residual Stress in Six-Particle Overlap Impact

Single-particle impact simulations reveal that the residual stresses are relaxed locally due to the nature of the interface bonding and that this effect is relatively greater in the particle. In this section, impacts of six particles on one another are simulated to further investigate the effects of subsequent impacts on interface bonding and the residual stress built-up. The proposed contact model is used for particle bonding in this study.

Figure 6 shows the step-by-step changes of the minimum principal stress along the symmetry axis of the system in the sequential impact of six identical particles. The relaxation effect on the compressive residual stress due to the interface bonding can be clearly seen in this

overlapping impact sequence. For example, the deposition of particle-2 relaxes the average compressive residual stress in particle-1 from -300 MPa (Fig. 6a) to around -150 MPa (Fig. 6b). The bonding of particle-3 relaxes the average residual stress in particle-2 from -250 MPa (Fig. 6b) to around -75 MPa (Fig. 6c). The deposition of particle-4 also relaxes the average residual stress in particle-3 from -100 MPa (Fig. 6c) to around -40 MPa (Fig. 6d).

The local environment of contact surfaces affects the relaxation near the interface. The interface bonding strongly affects the substrate for the first two impacts, where large changes in the residual stress can be seen in Fig. 6(a) and (b). Subsequent impacts have relatively minor effect on changing the residual stress distribution in the substrate. Instead, they significantly affect the residual stress distribution in the coating, for both already-deposited particles and impacting particles. It is interesting to see in Fig. 6(c)–(e) that the averaged residual stress in the impacting particles (e.g., particle-3 in Fig. 6c) seems to be stable at -150 MPa after their depositions. They differ from the averaged stress -300 to -200 MPa for the first two particles. With this relatively stable residual stress distribution in the impacting particles and the associated relaxation effect on the already-deposited particles, the average residual stress (minimum principal stress) throughout the coating (~ 25 μm) is predicted to be

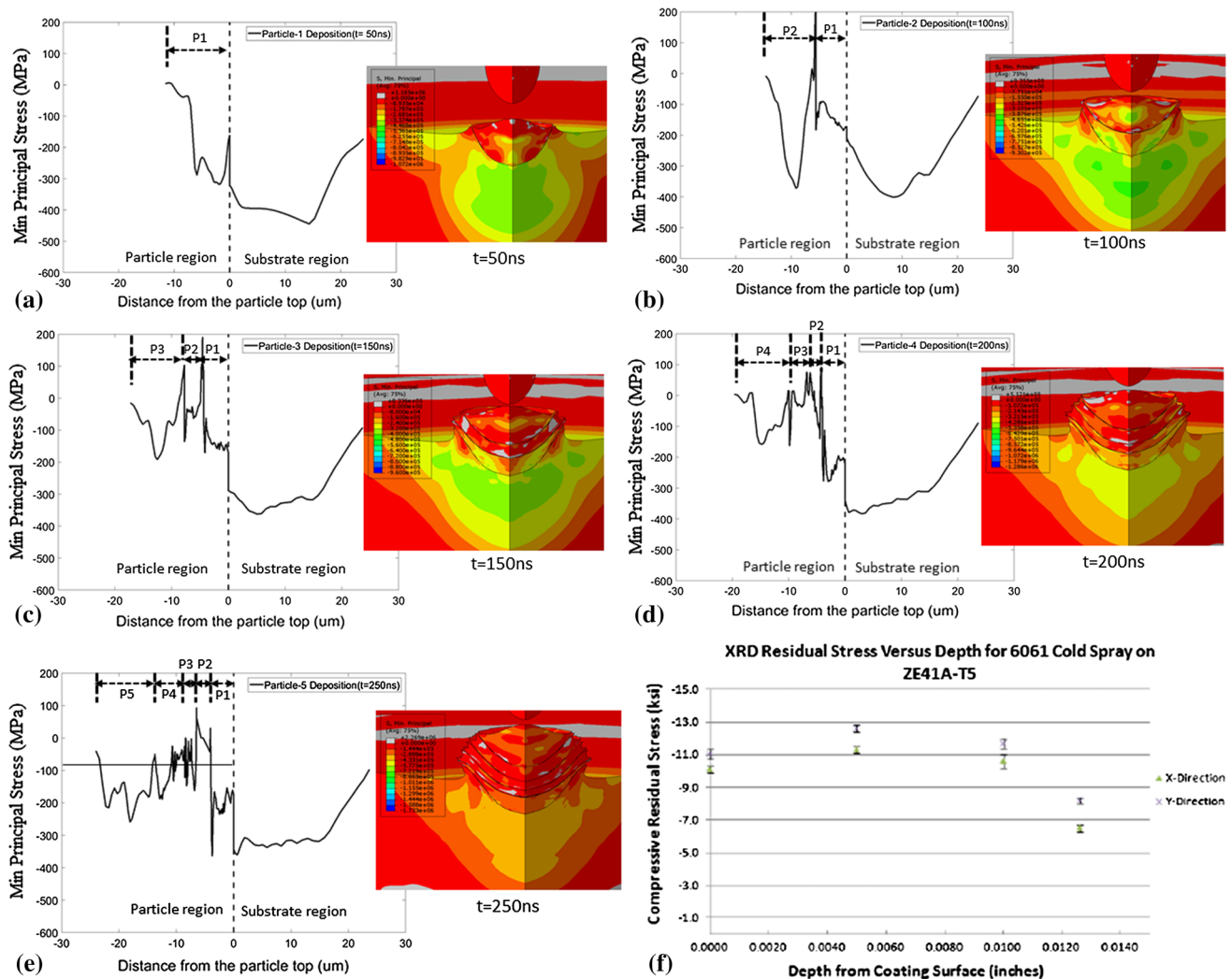


Fig. 6 (a)–(e) Step-by-step evolution of residual stress along the symmetry axis in the sequential impact of six particles and (f) the measured residual stress in Al6061 coating on a Mg substrate (Ref

around -100 MPa (Fig. 6e). Though only five-particle deposition is shown in Fig. 6, it is expected that the subsequent particles follow the same patterns of particle-3, particle-4 and particle-5 to influence the residual stress built-up.

The numerically predicted residual stress is compared with a measured stress distribution (Ref 23) in a coating of Al6061 powders coated on Mg substrate in Fig. 6(f). It is encouraging to see that the simulated residual stress of -100 MPa (-14.5 ksi) within a coating thickness of $25\ \mu\text{m}$ (0.001 in), is close to the XRD measured results of -75 to -90 MPa (-11 to -13 ksi) within a coating thickness of $125\ \mu\text{m}$ (0.005 in). It is worth pointing out that this comparison is made on the top of the coating region; therefore, the influence of substrate is expected to be negligible as explained above.

29). The gray color in contours (a)–(e) represents the tensile stress while other colors represent compressive stress

The development of residual stresses can also be seen from the time histories of particle impacts. Figure 7 shows the time evolution of minimum and maximum principal stresses at the contact center of the substrate and the particle-1 (see insert in Fig. 7a). As expected, the peening and interface bonding effects (arrows in Fig. 7a), which can be identified as that in Fig. 5(d), gradually fade away as the “coating” grows. This, again, reflects the local nature of these effects. In general, the peening effect tends to result in a compressive residual stress in the system, while the interface bonding effect tends to relax this compressive stress. The balance of these two effects following the impact of each particle determines the development of the final residual stress state. In Fig. 7, we see that this balance, which may strongly depend on the bonding conditions, could play either a positive, neutral or negative role to increase or decrease the local residual stress during each

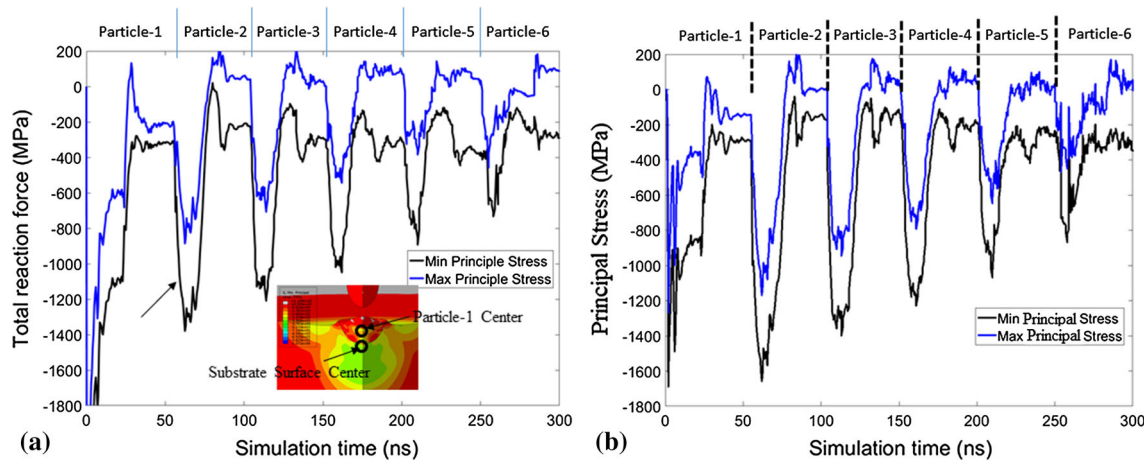


Fig. 7 Time history of principal stresses at the impact center (a) on the substrate and (b) on the particle-1 during subsequent impacts of six particles

particle's impact. This discussion indicates that the interface bonding should be considered as one of the essential factors in determining the final residual stresses in the numerical simulations.

Residual Stress in Multi-particle Random Impact

Multi-particle impact simulations are performed to investigate the residual stress built-up. Considering the expensive computational cost involved in the interface bonding, the surface-based cohesive model built-in ABAQUS (Ref 15) rather than the proposed surface contact model is used in this simulation. The cohesive strength σ_0 and damage evolution energy G are set as 350 MPa and 0.5 J/m² in the surface-based cohesive model. They are chosen according to the tensile strength and the grain boundary energy of Al6061, respectively.

Figure 8 shows a cutout view of the coating for the distributions of the minimum and maximum principal stresses. As expected, the stress state is mainly compressive in the substrate, below the impact area. The coating thickness affects the magnitude of the compressive stress in substrate. Larger compressive stresses under the coating periphery than those under the coating center are observed in Fig. 8(a). This, to some extent, can be attributed to the particle size in these two regions. The coating center generally has larger particles. Due to slower impact velocity (Eq 2) and weaker peening effect [with reduced kinetic energy per unit area on the substrate surface (Ref 30)], lower compressive residual stress is built-up under the coating center. Besides the particle size, the relaxation effect due to the interface bonding may also contribute to the differences in the compressive residual stress in these two regions.

The through-depth residual stresses in the substrate are plotted along the central axis in Fig. 8(c). The minimum principal stresses within the 100 μm depth are all in compression. They are not only well comparable with the XRD residual stress of Al6061 substrate coated by Al7075 measured by Ghelichi et al. (Ref 13) (black lines in Fig. 8d), but also match with their FEM simulation result before annealing (dash blue line in Fig. 8d). The maximum compressive stress obtained in current simulation is about -350 MPa, while it is -300 MPa in Ghelichi et al.'s measurements. The positive maximum principal stresses are observed at the substrate center near the surface. This is not unexpected since the interface bonding tends to relax the maximum principal stress into tensile, as seen in Fig. 7(a). In addition, these direction-related tensile residual stresses at substrate surface are also reported in Rokni et al.'s XRD measurements (Ref 7) and Saleh et al.'s neutron diffraction measurements (Ref 12) on Al6061 substrate. It is also worth noting that the minimum principal stress observed in the coating region (-80 MPa to -220 MPa, Fig. 8a) is also well comparable with Ghelichi et al.'s XRD measurements (-50 MPa to -200 MPa, black lines in Fig. 8d).

Conclusions

The residual stress evolution during cold spray coating process has been studied through single-, six- and multi-particle impact simulations. The influence of interface bonding on the residual stress is investigated.

Each individual impact event in cold spray coating process can be divided into three steps: the transient shock step, the peening and bonding step and the thermal cooling step. In the peening and bonding step, the peening effect

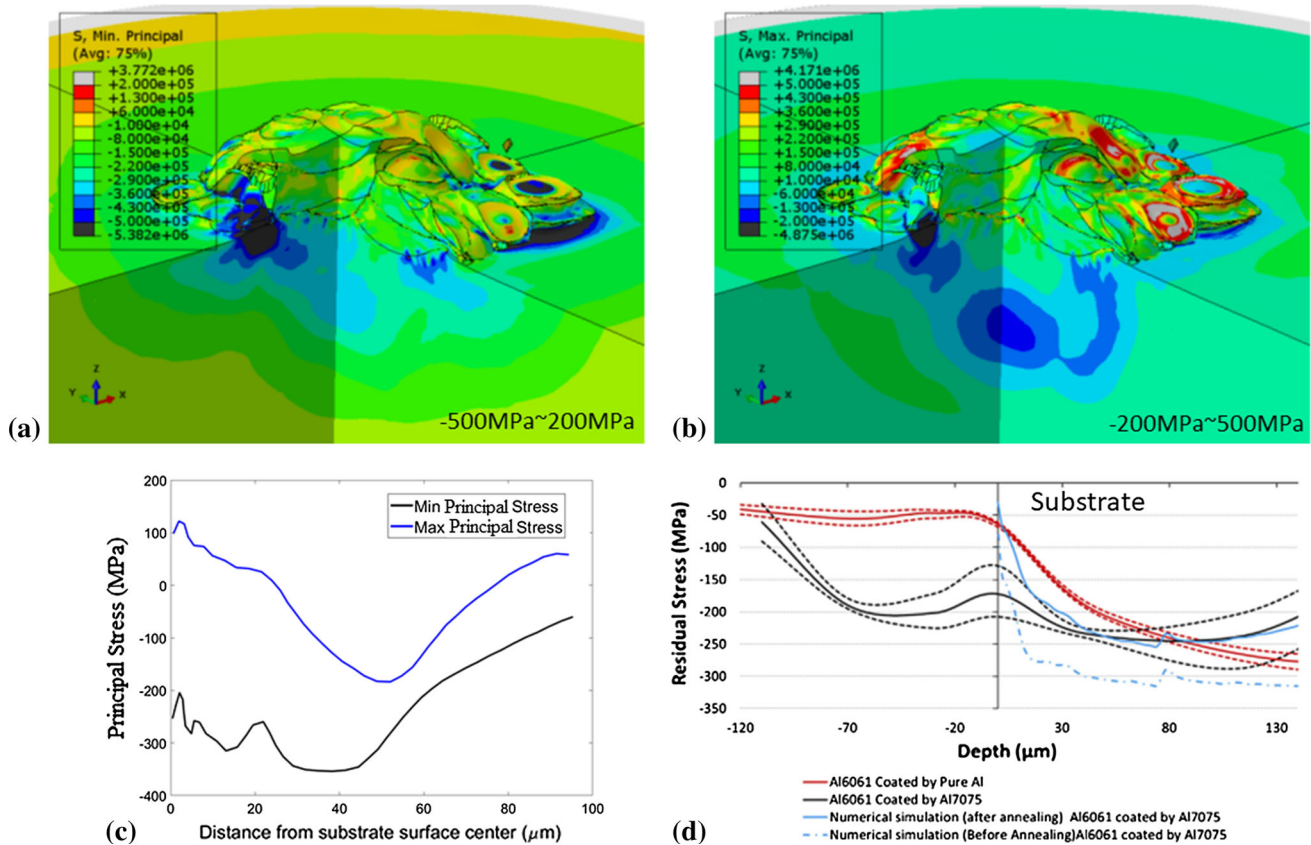


Fig. 8 (a) Minimum and (b) maximum principal stress distributions in the multi-particle random impact simulation; (c) the associated principal stress distributions in the substrate along the center symmetry axis and (d) averaged residual stress measured by Ghelichi

that is due to particle bombardment generally results in a compressive residual stress in the system, while the interface bonding as a result of surface traction generally serves to relax the compressive stress. The interface bonding mainly affects the local residual stress distributions at the interface region. During the cooling step, without considering the gas heating effect, the influence of temperature on the residual stress evolution depends on the material combination and their initial temperature differences. Due to the use of same material pairs (with identical thermal properties) and same initial temperature for the particle and the substrate, in current simulations, the temperature due to plastic heating is found to have a negligible effect on the residual stress evolution.

The balance between the peening and the bonding effects following each impact determines the final residual stress in the system. Their influences on the residual stress evolution depend strongly on the local bonding environment and could play either a positive, neutral or negative role to increase or decrease the previously developed residual stress during each particle impacts. Therefore, the interface bonding should be considered as one of the

essential factors in numerical simulations of residual stresses evolution in cold spray coating process.

With an appropriate interface bonding model, the numerical simulations can reasonably estimate the final residual stress built-up in both the substrate and the coating. The computed residual stresses are comparable with the experimental measurements. The agreements should be further verified by carefully matching the simulated impact conditions with the spray parameters in experiments.

Acknowledgment This work was sponsored in part by the Army Research Laboratories under the Grant Number W911NF-15-2-0026. Any opinions, findings and conclusions or recommendations expressed in this material are those of the author(s) and do not necessarily reflect the views of the US Government.

Appendix

The proposed surface contact model (Fig. 3) is implemented in ABAQUS/Explicit through a user subroutine VUINTERACTION. To verify the implementation, the separation-traction history for the contact pair between

south pole of the particle and center point of the substrate in the cohesive region ($\delta_n > 0$) is monitored throughout the single-particle impact simulation, as shown in Fig. S1. Each black circle in Fig. S1 represents the separation-traction relationship at the monitored simulation time step. It is clearly seen that the traction follows the assumed bilinear cohesive behaviors with δ_n , as expected. The values of the monitored cohesive stiffness $k_{\text{coh}} = 10^{11}$ MPa/mm, cohesive strength $\sigma_0 = 325$ MPa and cohesive damage energy $G = 1.0$ J/m² are exactly the same as those that are input to the code (listed in Table 1). In Fig. S1, it is also seen that after the onset of cohesive damage ($\sigma_t^n > \sigma_0$ or $\delta_n > \delta_{nc}$), the traction follows the degraded k_{coh} to load and unloading with δ_n until its final failure.

References

1. H. Assadi, F. Gärtner, T. Stoltenhoff, and H. Kreye, Bonding Mechanism in Cold Gas Spraying, *Acta Mater.*, 2003, **51**, p 4379–4394
2. T. Schmidt, F. Gärtner, H. Assadi, and H. Kreye, Development of a Generalized Parameter Window for Cold Spray Deposition, *Acta Mater.*, 2006, **54**, p 729–742
3. R. Ghelichi, D. MacDonald, S. Bagherifard, H. Jahed, M. Guagliano, and B. Jodoin, Microstructure and Fatigue Behavior of Cold Spray Coated Al5052, *Acta Mater.*, 2012, **60**, p 6555–6561
4. C.W. Ziemian, M.M. Sharma, B.D. Bouffard, T. Nissley, and T.J. Eden, Effect of Substrate Surface Roughening and Cold Spray Coating on the Fatigue Life of AA2024 Specimens, *Mater. Des. (1980-2015)*, 2014, **54**, p 212–221
5. Z. Arabgol, H. Assadi, T. Schmidt, F. Gärtner, and T. Klassen, Analysis of Thermal History and Residual Stress in Cold-Sprayed Coatings, *J. Therm. Spray Technol.*, 2014, **23**, p 84–90
6. T. Suhonen, T. Varis, S. Dosta, M. Torrell, and J.M. Guilemany, Residual Stress Development in Cold Sprayed Al, Cu and Ti Coatings, *Acta Mater.*, 2013, **61**, p 6329–6337
7. M.R. Rokni, C.A. Widener, O.C. Ozdemir, and G.A. Crawford, Microstructure and Mechanical Properties of Cold Sprayed 6061 Al in As-Sprayed and Heat Treated Condition, *Surf. Coat. Technol.*, 2017, **309**, p 641–650
8. G. Shayegan, H. Mahmoudi, R. Ghelichi, J. Villafuerte, J. Wang, M. Guagliano et al., Residual Stress Induced by Cold Spray Coating of Magnesium AZ31B Extrusion, *Mater. Des.*, 2014, **60**, p 72–84
9. V. Luzin, K. Spencer, and M.X. Zhang, Residual Stress and Thermo-mechanical Properties of Cold Spray Metal Coatings, *Acta Mater.*, 2011, **59**, p 1259–1270
10. K. Spencer, V. Luzin, N. Matthews, and M.X. Zhang, Residual Stresses in Cold Spray Al Coatings: The Effect of Alloying and of Process Parameters, *Surf. Coat. Technol.*, 2012, **206**, p 4249–4255
11. S. Rech, A. Trentin, S. Vezzù, J.-G. Legoux, E. Irissou, and M. Guagliano, Influence of Pre-Heated Al 6061 Substrate Temperature on the Residual Stresses of Multipass Al Coatings Deposited by Cold Spray, *J. Therm. Spray Technol.*, 2011, **20**, p 243–251
12. M. Saleh, V. Luzin, and K. Spencer, Analysis of the Residual Stress and Bonding Mechanism in the Cold Spray Technique Using Experimental and Numerical Methods, *Surf. Coat. Technol.*, 2014, **252**, p 15–28
13. R. Ghelichi, S. Bagherifard, D. MacDonald, I. Fernandez-Pariente, B. Jodoin, and M. Guagliano, Experimental and Numerical Study of Residual Stress Evolution in Cold Spray Coating, *Appl. Surf. Sci.*, 2014, **288**, p 26–33
14. W. Li, K. Yang, D. Zhang, and X. Zhou, Residual Stress Analysis of Cold-Sprayed Copper Coatings by Numerical Simulation, *J. Therm. Spray Technol.*, 2016, **25**, p 131–142
15. ABAQUS/CAE User's Manual: Version 6.13 (ABAQUS, Pawtucket, 2012)
16. O.C. Ozdemir, C.A. Widener, D. Helfrich, and F. Delfanian, Estimating the Effect of Helium and Nitrogen Mixing on Deposition Efficiency in Cold Spray, *J. Therm. Spray Technol.*, 2016, **25**, p 660–671
17. G.R. Johnson and W.H. Cook, A Constitutive Model and Data for Metals Subjected to Large Strains, High Strain Rates, and High Temperatures, in *Proceedings 7th International Symposium on Ballistics* (1983), pp. 541–547
18. A. Alizadeh Dehkharghani, *Tuning Johnson–Cook Material Model Parameters for Impact of High Velocity, Micron Scale Aluminum Particles*. Master Thesis (Northeastern University, Boston, 2016)
19. W. Xie, A. Alizadeh-Dehkharghani, Q. Chen, V.K. Champagne, X. Wang, A.T. Nardi et al., Dynamics and Extreme Plasticity of Metallic Microparticles in Supersonic Collisions, *Sci. Rep.*, 2017, **7**, p 5073
20. M.A. Meyers, *Plastic Deformation at High Strain Rates. Dynamic Behavior of Materials*, Wiley, New York, 2007, p 323–381
21. JAHM Software Inc., *Material Properties Database*. MPDB (2003); V7.01 demo
22. B. Yildirim, S. Muftu, and A. Gouldstone, Modeling of High Velocity Impact of Spherical Particles, *Wear*, 2011, **270**, p 703–713
23. G.R. Johnson and W.H. Cook, Fracture Characteristics of Three Metals Subjected to Various Strains, Strain Rates, Temperatures and Pressures, *Eng. Fract. Mech.*, 1985, **21**, p 31–48
24. A. Manes, D. Lumassi, L. Giudici, and M. Giglio, An Experimental-Numerical Investigation on Aluminium Tubes Subjected to Ballistic Impact with Soft Core 7.62 Ball Projectiles, *Thin Walled Struct.*, 2013, **73**, p 68–80
25. M. Hassani-Gangaraj, D. Veysset, K.A. Nelson, and C.A. Schuh, In-Situ Observations of Single Micro-particle Impact Bonding, *Scr. Mater.*, 2018, **145**, p 9–13
26. V.V. Bulatov, B.W. Reed, and M. Kumar, Grain Boundary Energy Function for FCC Metals, *Acta Mater.*, 2014, **65**, p 161–175
27. B. Yildirim, H. Fukunuma, T. Ando, A. Gouldstone, and S. Müftü, A Numerical Investigation Into Cold Spray Bonding Processes, *J. Tribol.*, 2014, **137**, p 011102–011113
28. S. Müftü, S. Zhalehpour, A. Gouldstone, and T. Ando, Assessment of Interface Energy in High Velocity Particle Impacts, in *38th Annual Meeting of The Adhesion Society*. Savannah, GA (2015)
29. B.M. Gabriel, V.K. Champagne, P.F. Leaman, and D.J. Helfrich, *Cold Spray for Repair of Magnesium Components*. Army Research Library Report No ARL-TR-6629 (2013)
30. S. Kikuchi, Y. Hirota, and J. Komotori, Effects of Particle Size for Peening on Microstructural Changes in Steel, *J. Jpn. Soc. Abras. Technol.*, 2010, **54**, p 720–724